Am J Physiol Lung Cell Mol Physiol 331: L92–L104, 2026.
First published June 9, 2026; doi:10.1152/ajplung.00002.2026

american physiological society

AMERICAN JOURNAL OF PHYSIOLOGY
LUNG CELLULAR AND MOLECULAR PHYSIOLOGY

RESEARCH ARTICLE

A biomimetic miniaturized in vitro model to target early markers of neonatal pulmonary vascular injury

Motaharehsadat Heydarian,[1,2] Ali Doryab,[1,2] Juan Henao,[3] Benjamin Schubert,[3] Otmar Schmid,[1] and Anne Hilgendorff[1,4,5]

[1]*Institute for Lung Health and Immunity and Comprehensive Pneumology Center, Helmholtz Zentrum München, Munich, Germany;* [2]*Department of Medicine, Addenbrooke's Hospital, University of Cambridge, Cambridge, United Kingdom;* [3]*Institute for Computational Biology, Helmholtz Zentrum München, Munich, Germany;* [4]*Dr. von Hauner Children's Hospital, University Hospital Ludwig-Maximilian University, Munich, Germany; and* [5]*Section of Neonatology, Pediatric Intensive Care, Pediatric Cardiology, Department of Paediatrics, School of Medicine and Health Sciences, Pediatric Pneumology and Allergology, and Research Centre Neurosensory Science, Carl von Ossietzky University, Oldenburg, Germany*

Abstract

Pulmonary vascular disease (PVD) is a major contributor to morbidity in preterm infants as it is associated with a significant risk to develop pulmonary hypertension, especially in infants diagnosed with prematurity-associated lung disease (PLD), also known as bronchopulmonary dysplasia (BPD). However, the earliest events of vascular injury triggered by postnatal mechanical and oxygen-related stress remain poorly understood, largely due to the limitations of existing in vitro models. We therefore developed a biomimetic, miniaturized pulmonary in vitro perfusion (PIPE) system that integrates pathophysiologically relevant shear stress with controlled oxygen exposure for the exposure of a human coculture of pulmonary microvascular endothelial cells and pulmonary artery smooth muscle cells. Advancing the system to a triple coculture, circulating THP-1 monocytes capture early endothelial-smooth muscle-immune cell interactions. Shear stress alone induced early proliferative and extracellular matrix-related responses in endothelial cells and resulted in enhanced monocyte recruitment without disrupting barrier integrity. When combined with oxygen exposure, the model revealed a dose-dependent injury pattern: moderate hyperoxia [fraction of inspired oxygen ($F_{I_{O_2}}$ = 0.40)] had minimal acute effects, whereas severe hyperoxia ($F_{I_{O_2}}$ = 0.85) impaired endothelial barrier function, increased reactive oxygen species (ROS) production, promoted monocyte transmigration, activated apoptosis (caspase 3), and elevated soluble collagen synthesis. This dynamic in vitro system reveals early drivers in vascular injury and recapitulates key characteristics of PVD, thereby introducing a translational platform for the dissection of disease mechanisms and evaluation of therapeutic strategies targeting vascular injury in the developing lung.

NEW & NOTEWORTHY We present a biomimetic, miniaturized in vitro model that replicates key features of neonatal pulmonary vascular injury. By integrating physiologically relevant cues, this platform enables early detection of injury-associated molecular markers and mechanistic interrogation of disease onset. This scalable model offers a powerful tool for studying neonatal lung vascular pathology and for accelerating the discovery of early diagnostic and therapeutic strategies.

biomimetic in vitro perfusion model; bronchopulmonary dysplasia; pulmonary vascular disease; shear stress; vascular injury

INTRODUCTION

Preterm birth, affecting nearly 10% of all live births, renders the immature lung highly susceptible to postnatal injury. Lifesaving interventions such as mechanical ventilation and oxygen therapy (1, 2), together with pre- or postnatal infection, are known to disrupt alveolar and vascular development (3, 4). The subsequent development of prematurity-associated lung disease (5) or bronchopulmonary dysplasia (BPD) is inextricably linked to lifelong impairment, including a substantial risk for the development of pulmonary hypertension (PH) (6, 7). A key but often underrecognized component of BPD pathophysiology is pulmonary vascular disease (PVD). Here, the immature, structurally limited vascular bed is abruptly exposed to full systemic blood flow, hemodynamic stressors (e.g., patent ductus arteriosus and parenteral fluids), fluctuating oxygen levels, and mechanical forces introduced by artificial ventilation (8–10). Together, these stressors trigger endothelial injury, inflammation, and remodeling, including excessive extracellular matrix (ECM) deposition and smooth muscle thickening (11). PVD affects all infants with BPD to a varying degree, often escapes clinical monitoring, but results in an up to 30%

Correspondence: A. Hilgendorff (anne.hilgendorff@uni-oldenburg.de); M. Heydarian (mh2348@cam.ac.uk).
Submitted 2 January 2026 / Revised 23 April 2026 / Accepted 1 June 2026

risk for the development of PH in infants with moderate and severe BPD (12).

Despite its clinical relevance, the earliest and potentially preventable events underlying postnatal vascular injury remain poorly understood. On the one hand, existing models rarely capture the early events of pathologic endothelial-smooth muscle interactions. On the other hand, most models rely on maximized oxygen concentrations while overlooking the double-hit injury provoked by shear stress in the presence of clinically relevant, moderate hyperoxia (13–15). This creates a critical gap in understanding how postnatal mechanical and oxygen-related cues jointly shape early PVD.

We therefore developed a miniaturized pulmonary in vitro perfusion (PIPE) system that applies controlled, perfusion-generated disease-relevant shear stress to human primary microvascular endothelial cells (hPMECs) and pulmonary artery smooth muscle cells (hPASMCs) at levels relevant to the microvasculature of the developing lung, while enabling precise manipulation of oxygen exposure features not attainable in conventional culture systems. The applied wall shear stress (WSS) levels were derived from clinical data and previously published models (16, 17).

We then recreated innate immunovascular interactions under dynamic flow in a triple coculture model by circulating monocytic THP-1 cells, known to play a critical role in neonatal lung inflammation and PVD (18–20). Exposure of the triple coculture to room air ($FI_{O_2} = 0.21$), clinically prevalent moderate hyperoxia [fraction of inspired oxygen ($FI_{O_2} = 0.40$)], or severe hyperoxia ($FI_{O_2} = 0.85$) under dynamic flow conditions in comparison with static flow allowed us to identify critical events of early microvascular injury. We successfully demonstrate that shear stress alone induces early proliferative and ECM-related responses in vascular cells and enhances monocyte recruitment. In this context, hyperoxia acted in a dose-dependent manner: moderate concentrations had limited acute effects, whereas severe hyperoxia triggered impaired barrier integrity, increased reactive oxygen species (ROS) production, heightened monocyte transmigration, apoptosis, and early collagen synthesis. Key observations were validated in a preclinical mouse model following neonatal hyperoxia exposure into adolescence.

Taken together, these data identify the earliest events of vascular injury, including immune alterations during postnatal injury, and establish the PIPE platform as a biomimetic, translationally relevant system for dissecting the mechanisms underlying BPD-associated PVD.

MATERIALS AND METHODS

Design and Fabrication of the Pulmonary In Vitro Perfusion System

This study used an in-house multiwell pulmonary in vitro perfusion (PIPE) millifluidic system. The setup consists of five independent miniaturized bioreactors that run in parallel and are connected to a central chamber and reservoir. The main chamber is divided into basal and apical compartments by a polycarbonate membrane. In the main chamber, an interface (outlet) connects the apical compartment to the air-tight container to control temperature, humidity, and oxygen concentration. The culture medium in the basal compartment was circulated to simulate blood flow with a peristaltic pump (Shenzhen LabVI-II). Once the cell cultures were established, they were transferred to the PIPE system and subjected to quasicontinuous, unidirectional flow generating shear stress. Static culture conditions were used as a comparator to widely used conventional cell culture models operating without flow. For oxygen exposure experiments, the PIPE setup was placed in an airtight container connected to an oxygen concentrator, generating oxygen concentrations with a fraction of inspired oxygen (FI_{O_2}) of 0.21, 0.40, and 0.85, respectively. Oxygen concentrations were monitored using an oxygen meter (Greisinger Instruments; oxygen sensor GOEL 381; Fig. 1*B*).

Computational Shear Stress Simulation

Wall shear stress (WSS) on endothelial cells cultured on the basal side of a Transwell insert was simulated using COMSOL Multiphysics (v.6.3). A two-dimensional (2-D) rectangular domain (6.5 × 0.4 mm) representing the flow channel beneath the cell layer was modeled with steady-state, incompressible, laminar Navier–Stokes equations. The culture medium was treated as a Newtonian fluid [density 1,000 kg/m^3, viscosity (μ) 0.93 mPa·s (21)]. A uniform inlet velocity corresponding to a perfusion rate of 2 mL/min (Q) was applied, with zero pressure at the outlet and no-slip conditions at the top (cell surface) and bottom walls.

The domain was meshed with boundary layer refinement at the cell layer, and a stationary solver was used to compute velocity and shear stress. WSS on the endothelial monolayer was calculated (*Eq. 1*) from the viscous stress tensor, and average WSS was obtained via line integration along the cell-covered boundary:

$$\mathrm{WSS} = \frac{6\,\mu Q}{wh^2} \qquad (1)$$

Primary Human Cell Sources and Cell Lines

Primary human pulmonary microvascular endothelial cells (hPMEC) (Promo Cell, Cat. No. C-12282) were cultured in endothelial cell growth medium MV (Promo Cell, Cat. No. C-22020). Primary human pulmonary artery smooth muscle cells (hPASMC) (ThermoFisher, Cat. No. C0095C) were cultured in SmGMTM-2 smooth muscle cell growth medium-2 BulletKitTM (Lonza, CC-3182). Human monocytic cell line (THP1) (BIOZOL, Cat. No. ADD-C0003024) was cultured in RPMI-1640 (Gibco/Thermo Fisher Scientific, Cat. No. 11875093) supplemented with 10% heat-inactivated fetal calf serum (FCS; Sigma/Merck) and 1% penicillin/streptomycin (Gibco/Thermo Fisher Scientific). Human endothelial EA.hy926 cells [CRL-2922, American Type Culture Collection (ATCC)] were maintained in DMEM/F12 (Gibco/Thermo Fisher Scientific). Supplemented with 10% FCS (Sigma/Merck) and 1% penicillin/streptomycin (Gibco/Thermo Fisher Scientific).

Establishment of Coculture and Triple Coculture Models

Transwell inserts (6.5 mm diameter with 5.0 µm pore polycarbonate membrane; Merck Corning, Cat. No. CLS3421)

were coated with 50 µL of 1:1 collagen-fibronectin solution (Collagen I, rat tail, Cat. No. A1048301) and fibronectin (Cat. No. 10838039001, Sigma) from the basal side. The inserts stayed under the hood for air drying. hPMECs were seeded on the basal side of the membranes (cell density: 0.025×10^6) and incubated (37°C, 95% humidity, and CO_2 concentration of 5%) overnight. Next, hPASMCs were seeded on the apical side of the membranes (cell density: 0.025×10^6). With a seeding density of 1:1, an optimal cell proliferation rate was achieved. The cell models were kept in a 1:1 coculture medium for 5 days until cell layers were fully confluent, based on barrier integrity evaluation. When cocultures were established in the microfluidic system, the human monocytic cell line (THP1 cells, density: 0.6×10^6) was added to the reservoir facing the hPMECs side of the membrane in a 1:1:1 triple coculture medium for 8 h. The culture medium was supplemented with HEPES buffer to maintain a stable pH throughout the experiments.

Apparent Permeability

To determine the apparent permeability, we added 200 and 500 µL of fluorescein isothiocyanate dextran (FITC-dextran 4 kDa, Sigma Aldrich), and DMEM/F-12, phenol red-free (Thermo Fisher) to the apical (donor) and basal (recipient) compartments, respectively. The basal compartment in a black 96-well plate was sampled every 30 min. The culture media was replaced with an equal amount. The samples were analyzed using a plate reader (Safire 2, Tecan) at excitation and emission wavelengths of 483 and 525 nm, respectively. We calculated the apparent permeability coefficient (P_{app}, cm/s) using *Eq. 2* (22, 23), where dQ/dt is the steady-state flux or the transport rate, A is the surface area of the membrane (0.33 cm^2), and C_0 is the initial concentration of fluorescein sodium added to the apical compartment (mg/mL).

$$P_{app} = \frac{dQ}{dt} \times \frac{1}{(A \times C_0)} \quad (2)$$

Transmigration Assay

Cell tracker red CMTPX dye (Cat. No. C34552, Thermo Fisher) was used, according to the company protocol to monitor the THP1 monocytic cell line movement and location in relation to the hPMECs/hPASMCs coculture. In brief, the cells were harvested by centrifugation, and the supernatant was aspirated. Afterward, the THP1 monocytic cells were gently resuspended in a prewarmed CellTracker working solution, resuspended, and incubated for 15–45 min under growth conditions. Next, the THP1 monocytic cells were removed from the CellTracker working solution and resuspended in culture media. After loading the THP1 monocytic cells, the dye was well retained, allowing for tracking of cellular movements under the excitation and emission wavelengths of 577/602 nm.

Total Soluble Collagen Assay

Total soluble collagen content in total supernatants (coculture medium) was determined using Sircol colorimetric soluble collagen assay (Cat. No. S1000, Biocolor, UK), according to the manufacturer's instructions.

Nitric Oxide Assay

Nitric oxide (NO) production was measured in culture medium using Griess assay (Cat. No. BML-AK136, Enzo Life Sciences), according to the manufacturer's instructions.

Reactive Oxygen Species Assay

ROS levels in the models were measured using the Abcam ROS assay kit (ab186027) following the manufacturer's protocol. In brief, 300 µL of the diluted ROS detection dye was added to each well. After incubation for 30 min at room temperature, fluorescence was measured at 520/605 nm using a microplate reader.

Immunofluorescence

For immunofluorescence (IF), samples were fixed with 4% PFA, and incubated at 4°C overnight with primary antibodies CD144 (VE-cadherin) monoclonal Ab (1:100, mouse, Cat. No. 14–1449-82 eBioscience, Invitrogen), cleaved caspase-3 Ab (1:400, rabbit, Cat. No. 9661S, Cell Signaling), Ki67 monoclonal Ab (1:100, mouse, Cat. No. 14–5698-82, eBioscience, Invitrogen), and collagen type IV monoclonal Ab (1:100, mouse, Cat. No. 14–9871-82, eBioscience, Invitrogen), followed by secondary antibody incubation overnight. The secondary antibodies were Alexa Fluor 488 goat anti-mouse Ab (1:250, Cat. No. A-11001, Invitrogen), Alexa Fluor 568 goat anti-mouse Ab (1:250, Cat. No. A-11004, Invitrogen), Alexa Fluor Plus 488 goat anti-rabbit Ab (1:250, Cat. No. A32731, Invitrogen), and Alexa Fluor 568 goat anti-rabbit Ab (1:250, Cat. No. A-11011, Invitrogen). F-actin cytoskeleton and cell nucleus were stained using Alexa Fluor 488 Phalloidin (1:400, Cat. No. A12379, Invitrogen) and 4′,6-Diamidino-2-phenylindole (DAPI, 1:1,000, Cat. No. D9542, Sigma-Aldrich), respectively. Samples were embedded in Glycergel DAKO (Cat. No. S3023, Agilent). Images were acquired using Zeiss 880 upright confocal laser scanning microscopy (CLSM) coupled with ZEN Black 2.3 and processed using the three-dimensional (3D) reconstruction ImageJ/Fiji, v.2.3.0/1.53f, National Institutes of Health (NIH), Bethesda, MD (24). IF Images were reconstructed and processed using the 3-D IMARIS software (v.9.3.0; Bitplane, Zurich, Switzerland).

3′ Massive Analysis of cDNA Ends RNA Sequencing

On each side of the membranes, cells were trypsinized and lysed separately using the Trypsin-EDTA (0.25%) (Cat. No. 25200056, Gibco) and the RLT lysis buffer (Cat. No. 79216, Qiagen) for sample preparation. To ensure high separation efficiency, cell counts and fluorescent staining were performed postdetachment to confirm complete cell detachment. Samples were stored at −80°C and shipped to GenXPro GmbH on dry ice. The process of extraction of RNA from the cells, DNAase digestion, quality control, quantification (Fluorescence photometry, Qbit), cDNA synthesis, and barcoded MACE-Seq library preparation using TrueQuant adaptors and Illumina HiSeq2000 sequencing were done by GenXPro GmbH. Bioinformatic analysis, including raw data cleaning, TrueQuant bias elimination, and quantification for MACE, annotation to existing database entries, gene ontology annotation, and enrichment analysis, was done by GenXPro GmbH.

Animal Study

Pathogen-free C57BL/6 mice (male and female) were acquired from Charles River (Sulzfeld, Germany) and housed at constant temperature and humidity, a 12-h light cycle, and food and water ad libitum as described previously (10). After spontaneous delivery, newborn mice (3.3 ± 0.5 g body wt.) were randomly assigned to postnatal treatment on postnatal *days 5–7*. Following randomization, the pups received oxygen (O_2) with FI_{O_2} of 0.4 or 0.85 for 8 h or spontaneously breathed room air ($FI_{O_2} = 0.21$). Following hyperoxia treatment, neonatal mice were returned to the cage to stay with their mothers for 3 wk, i.e., exposure of the neonatal lung to injury was achieved in the saccular stage of lung development [ED 17.5 to postnatal *day 5* (P5) in mice; gestational age 27–36 wk in humans], whereas lungs were assessed after alveolarization took place. This design was chosen to *1*) align our in vivo studies with clinically relevant conditions and *2*) address sustained changes (10, 25). At the age of 26 ± 2 days, lungs were fixed intratracheally with 4% buffered PFA at 20 cmH_2O, and lung volumes were measured as described previously (26), demonstrating comparable results for all groups: $FI_{O_2} = 0.21$: 65 ± 7.0 μL^3; $FI_{O_2} = 0.4$ group: 66 ± 5.0 μL^3; $FI_{O_2} = 0.85$ group: 65 ± 14.0 μL^3 (means and SD each). All animal experiments followed strict governmental and international guidelines and were approved by the local government for the administrative region of Upper Bavaria Animal Care and Use Committee (TVA No. 55.2-1-54-2532-117-2010). Immunofluorescence staining of the paraffin-embedded lung tissue sections was performed as described earlier (10) using F4/80 (Cat. No. 16836155, Thermo Fisher Scientific) and cleaved caspase-3 Ab (1:400, rabbit, Cat. No. 9661S, Cell Signaling). Histology Van Gieson's trichrome staining was performed following the manufacturer's instructions (Carl Roth, Germany), followed by quantitative and qualitative assessment of microvessels (20–100 μm) as described previously (26). Images were acquired using a Zeiss Axio Scan Z.1 slide scanner (ZEISS).

Statistical Analysis

GraphPad Prism 10 for macOS v.10.3.1 (GraphPad Software, CA) was used to analyze the data. The figure legend provides specific details on the statistical analysis and the number of experiments conducted (n): $^*P < 0.05$, $^{**}P < 0.001$, $^{***}P < 0.0001$, and $^{****}P < 0.00001$. Differential expression analysis was performed using DESeq2 v.1.36.0 R package with P value correction by Benjamini–Hochberg. Genes with total counts < 10 were discarded, and FDR < 0.05 was chosen as the threshold for significance. Enrichment analysis was performed using gProfiler2 v.0.2.1 R package mapping for the Ensembl 109 database (Ensembl Genomes 56, built on 2022-03-29). REACTOME pathways with adjusted P value < 0.05 (gSCS method, by default) were considered significant. Volcano and bar plots for differential expression and enrichment analysis were created using internal R scripts based on the ggplot2 v.3.4.2 R package. The transcriptomics analysis and visualization scripts were carried out in R v.4.2.3.

RESULTS

Postnatally, the functionally and structurally immature microvasculature that characterizes the developing lung in preterm neonates is exposed to elevated mechanical forces, i.e., shear stress introduced by systemic stroke volumes and artificial ventilation (8). To investigate the earliest and previously uncharacterized effects of shear stress and hyperoxia on the lung microvasculature, we engineered and validated a multiwell, miniaturized biomimetic PIPE system. The platform incorporates a basal endothelial layer (hPMECs) cocultured with apical human pulmonary arterial smooth muscle cells (hPASMCs) and enables the controlled exposure to defined levels of shear stress (Fig. 1, *A* and *B*). In the next step, we advanced this system to allow the simultaneous regulation of perfusion and oxygen, thereby mimicking a clinically relevant postnatal treatment regimen (9, 27).

Successful Implementation of a Biomimetic Platform to Investigate Early Pathophysiologic Cues in Microvascular Injury

Computational flow simulations of the main chamber revealed a stable and spatially uniform velocity field across the channel (Fig. 1*Cii*), confirming that applying perfusion to the basal compartment produced consistent flow conditions along the endothelial monolayer. The velocity profile across the channel height (y-axis) demonstrated a symmetric parabolic distribution, characteristic of laminar flow, further supporting uniform shear delivery within the endothelial region. Correspondingly, wall shear stress (WSS) levels at the endothelial surface reached ~10.9 dyn/cm^2 under a perfusion rate of 2 mL/min (Fig. 1*Ciii*). This level is consistent with data obtained in pediatric patients with PH (16) and consistent with previously published models for human pulmonary endothelial cells (17).

To validate effective transmission of shear stress to adherent endothelial cells in the PIPE system, we cultured EA.hy926 cells on the basal surface of the Transwell membrane and exposed them to 24 h of controlled shear (10.9 dyn/cm^2). Endothelial cells exhibited marked alignment of the F-actin cytoskeleton in the direction of flow (Fig. 1*D*). Importantly, no evidence of cytotoxicity or compromised monolayer integrity was observed at this shear magnitude.

Successfully establishing a physiologically relevant human-based coculture model within the PIPE system, we cultured primary human pulmonary microvascular endothelial cells (hPMECs) and human pulmonary arterial smooth muscle cells (hPASMCs) on the basal and apical surfaces of ECM coated-Transwell inserts, respectively (Fig. 1*E*). Confocal imaging confirmed the formation of a confluent endothelial monolayer characterized by continuous VE-cadherin junctions and organized F-actin architecture, whereas hPASMCs formed a robust monolayer on the apical surface (Fig. 1*F*). Functional assessment of barrier integrity demonstrated a progressive decline in apparent permeability (P_{app}), decreasing from 8.4×10^{-6} cm/s on *day 1* to 2.6×10^{-6} cm/s by *day 5* ($P < 0.0001$), consistent with formation of the endothelial barrier (Fig. 1*G*). Importantly, permeability remained stable thereafter, with no significant difference between *days 5* and *6* ($P = 0.884$), indicating that the coculture model maintains barrier integrity under extended culture conditions.

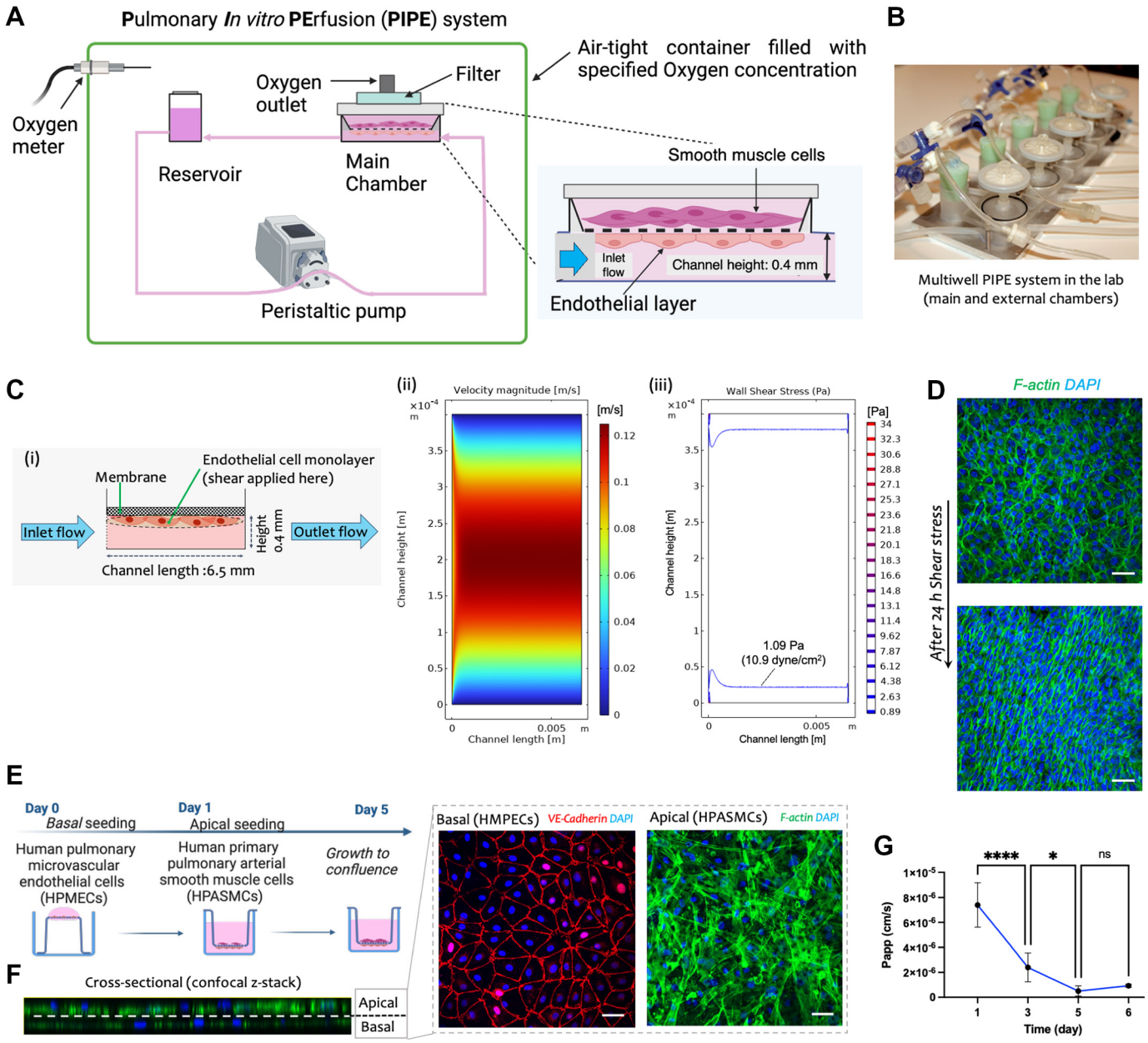

Figure 1. Concept and characterization of the biomimetic pulmonary in vitro perfusion (PIPE) system for investigating shear stress and oxygen exposure as a model of pulmonary vascular disease (PVD). *A*: schematic of the PIPE platform, consisting of a main chamber and an external medium reservoir connected in a closed perfusion loop. Cell culture inserts are housed within the main chamber, where culture medium is continuously perfused using a peristaltic pump to apply controlled shear stress to the basal surface of the cell model. All cells were maintained in fully submerged conditions. The apical compartment is connected to an air-tight container that enables precise control of temperature, humidity, and oxygen concentration. *B*: representative photograph of the multiwell PIPE system, showing both the main chambers and the external reservoirs. *C*: computational modeling of shear stress within the main chamber; (*i*) schematic of the transwell-based flow channel used for simulations; (*ii*) simulated velocity profile across the channel; and (*iii*) line profile of wall shear stress (WSS) at the endothelial cell surface. Simulations were performed using the following parameters: flow rate 2 mL/min, channel length 6.5 mm, and channel height 0.4 mm. The resulting WSS was ~1.09 Pa (10.9 dyn/cm^2). Flow was generated using a peristaltic pump, resulting in quasicontinuous flow with inherent low-amplitude pulsatility. *D*: immunofluorescence images of EA.hy926 endothelial monolayers cultured on the *bottom* (basal) side of the transwell insert and exposed to 24 h of shear stress, demonstrating alignment of the F-actin cytoskeleton (*green*) in the direction of flow. Nuclei are stained with DAPI (blue). *E*: workflow for establishing the PIPE coculture model using primary human pulmonary microvascular endothelial cells (hPMECs; basal side) and primary human pulmonary arterial smooth muscle cells (hPASMCs; apical side), expanded to confluence over 5 days. *F*: confocal laser scanning microscopy (CLSM) images of the coculture model. XZ reconstruction (*left*) shows VE-cadherin (*red*) localized at endothelial cell junctions on the basal surface, and XY view (*right*) shows hPASMC organization on the apical surface. F-actin is stained with phalloidin (*green*), and nuclei with DAPI (*blue*). Scale bar: 50 μm. *G*: time-dependent measurements of apparent permeability (P_{app}, FITC-dextran 4 kDa) demonstrating formation of the endothelial/SMC barrier (means ± SD, $n = 6$ biological replicates). Statistical analysis was performed using one-way ANOVA with Tukey's post hoc test; *$P < 0.05$, ****$P < 0.0001$. DAPI, 4′,6-Diamidino-2-phenylindole; FITC, fluorescein isothiocyanate; ns: not significant; SMC, smooth muscle cells. Figure created with a licensed version of BioRender.com.

Shear Stress Provokes Early Vascular Injury and Remodeling in a Model of PVD, Together with Enhanced Monocyte Recruitment

Exposure of the hPMEC/hPASMC coculture model to a shear stress of 10.9 dyn/cm^2 for 8 h induced several notable biological responses compared with static culture conditions (Fig. 2). Shear stress significantly increased endothelial cell proliferation, as reflected by a higher proportion of Ki67$^+$ cells on the basal hPMEC layer (Fig. 2, *A* and *B*). In contrast, endothelial barrier function remained unchanged, with no significant differences in apparent permeability (P_{app}) between static and dynamic conditions (Fig. 2*E*; 8.5×10^{-7} vs. 1.1×10^{-6}, means ± SD, P value = 0.054). However, shear stress elicited a marked increase in nitrite secretion (Fig. 2*C*; 15.3 vs. 23.4, means ± SD, P value = 0.004) and elevated total soluble collagen production in endothelial and smooth muscle cells (Fig. 2*D*; 3.9 vs. 7.6, means ± SD, P value = 0.014), suggesting early extracellular matrix (ECM) remodeling.

To further dissect cell type-specific mechanobiological responses, we performed 3′ massive analysis of cDNA ends (MACE) RNA sequencing on isolated hPASMCs and hPMECs following shear exposure (Fig. 2*F*). Endothelial cells exhibited robust transcriptional activation, dominated by the upregulation of cytokine- and ECM-associated genes, consistent with the observed increases in nitrite and soluble collagen. Downregulated transcripts included key regulatory mediators such as *HSP90*, *CAVIN2*, and *CYP1A1*, indicating involvement of endothelial nitric oxide synthase (eNOS)- and cytochrome p450 signaling pathways. In parallel, hPASMCs displayed pronounced induction of inflammatory and matrix-related genes, including *TGFB1*, *IL1B*, and *COL6A*, alongside the repression of developmental regulators such as *TBX1*. Pathway enrichment using the Reactome database confirmed activation of cytokine signaling pathways (IL-4/IL-13 signaling) and ECM remodeling processes (collagen formation) in hPMECs, with hPASMCs exhibiting a highly overlapping profile characterized by upregulated collagen biosynthesis, integrin-mediated interactions, and fibrillar matrix organization (Fig. 2*F*).

When establishing a dynamic triple coculture by the successful introduction of circulating THP-1 monocytes alongside the endothelial layer (Fig. 2*G*), we were able to demonstrate that shear stress markedly enhanced THP-1 transmigration across the hPMEC barrier toward the hPASMC layer, as visualized by confocal imaging (Fig. 2*H*). The finding was confirmed by quantitative analysis (Fig. 2*I*), indicating increased monocyte recruitment and transmigration under conditions of shear stress, further contributing to the pattern of matrix remodeling and endothelial injury.

Severe but Not Moderate Hyperoxia Enhances Vascular Injury and Remodeling in the Context of Shear Stress in a Triple Coculture Model of PVD

Building on the established dynamic triple coculture model, we next sought to mimic postnatal exposure to clinically relevant oxygen levels by subjecting the system to normoxia (FI_{O_2} = 0.21), moderate (FI_{O_2} = 0.40), or severe hyperoxia (FI_{O_2} = 0.85) for 8 h in the presence of shear stress (Fig. 3*A*). In this double-hit model, exposure to moderate hyperoxia, reflecting oxygen levels commonly used in neonatal care, did not significantly alter endothelial barrier integrity (Fig. 3*B*), ROS generation (Fig. 3*C*), monocyte transmigration (Fig. 3, *D* and *E*), caspase-3 activity (Fig. 3, *F* and *G*), collagen IV deposition (Fig. 3*H*), or total soluble collagen levels (Fig. 3*I*), when compared with normoxia conditions in the triple coculture model. In contrast, severe hyperoxia (FI_{O_2} = 0.85) resulted in reduced barrier integrity and markedly increased ROS production (Fig. 3, *B*–*C*), accompanied by enhanced THP-1 monocyte transmigration across the endothelial layer (Fig. 3, *D* and *E*) when compared with normoxia. Severe hyperoxia also triggered a significant rise in caspase-3 expression (Fig. 3, *F* and *G*), indicating increased apoptotic activity, as well as elevated levels of total soluble collagen (Fig. 3*I*), suggestive of extracellular matrix remodeling. Collagen IV expression remained unchanged across all oxygen conditions (Fig. 3*H*).

In a preclinical model, we exposed neonatal mice at postnatal *days 5–7*, i.e., in the saccular stage of lung development (E17.5–P5; equivalent to human gestational age 27–36 wk) to moderate (FI_{O_2} = 0.40) or severe hyperoxia (FI_{O_2} = 0.85) for 8 h (27, 28). Severe hyperoxia led to enhanced monocyte/macrophage recruitment, induction of apoptosis, and collagen deposition in the alveolar area, together with a reduction in the number of small blood vessels (20–100 µm) 3 wk after exposure (Fig. 4, *A*–*E*). In contrast to severe hyperoxia, moderate oxygen supplementation induced only milder changes to monocyte recruitment, apoptosis, and collagen deposition, resulting in no significant changes to microvessel number. Although the animal experiments were performed to relate the effects observed in vitro to early changes following hyperoxia exposure in vivo and early signs of neonatal pulmonary injury, including effects on pulmonary microvessel density, macrophage infiltration, apoptosis, and collagen deposition, which reflect the pathologic hallmarks observed in vitro, the in vivo setting was not designed to exactly mirror the conditions applied in the in vitro PIPE setting.

DISCUSSION

"The severe impairment of vascular development is a central component of prematurity-associated lung disease (PLD) and is caused by multiple postnatal insults impacting the immature pulmonary vascular bed, ultimately promoting PVD" (5). The rise in vascular resistance due to microvessel rarefaction and progressive remodeling parallels clinical evidence of increased right ventricular afterload in infants with BPD (8, 29). Despite the clinical importance of PVD and its severe risk to progress into PH (30), the early drivers and pathophysiologic cues remain insufficiently understood, hindering the development of effective preventive or therapeutic strategies. We therefore developed an in vitro model designed to recapitulate key postnatal conditions, namely hemodynamic stimulation and hyperoxia, that the immature, rarefied vascular bed of the preterm lung is exposed to early after birth.

We established a human-based coculture of hPMEC/hPASMC with robust and comparable barrier integrity (31) on a porous membrane integrated into a millifluidic PIPE system that circulates medium across the basal (endothelial) compartment to generate quasicontinuous, unidirectional

flow and thereby shear stress (Fig. 1). In the study presented, static culture conditions were used as a comparator to widely used conventional cell culture models operating without flow, rather than a physiological baseline as the absence of flow does not reflect the native mechanical environment in the lung microvasculature. Future studies can, however, incorporate defined physiological and pathological hemodynamic regimes, such as variations in shear stress magnitude, to better

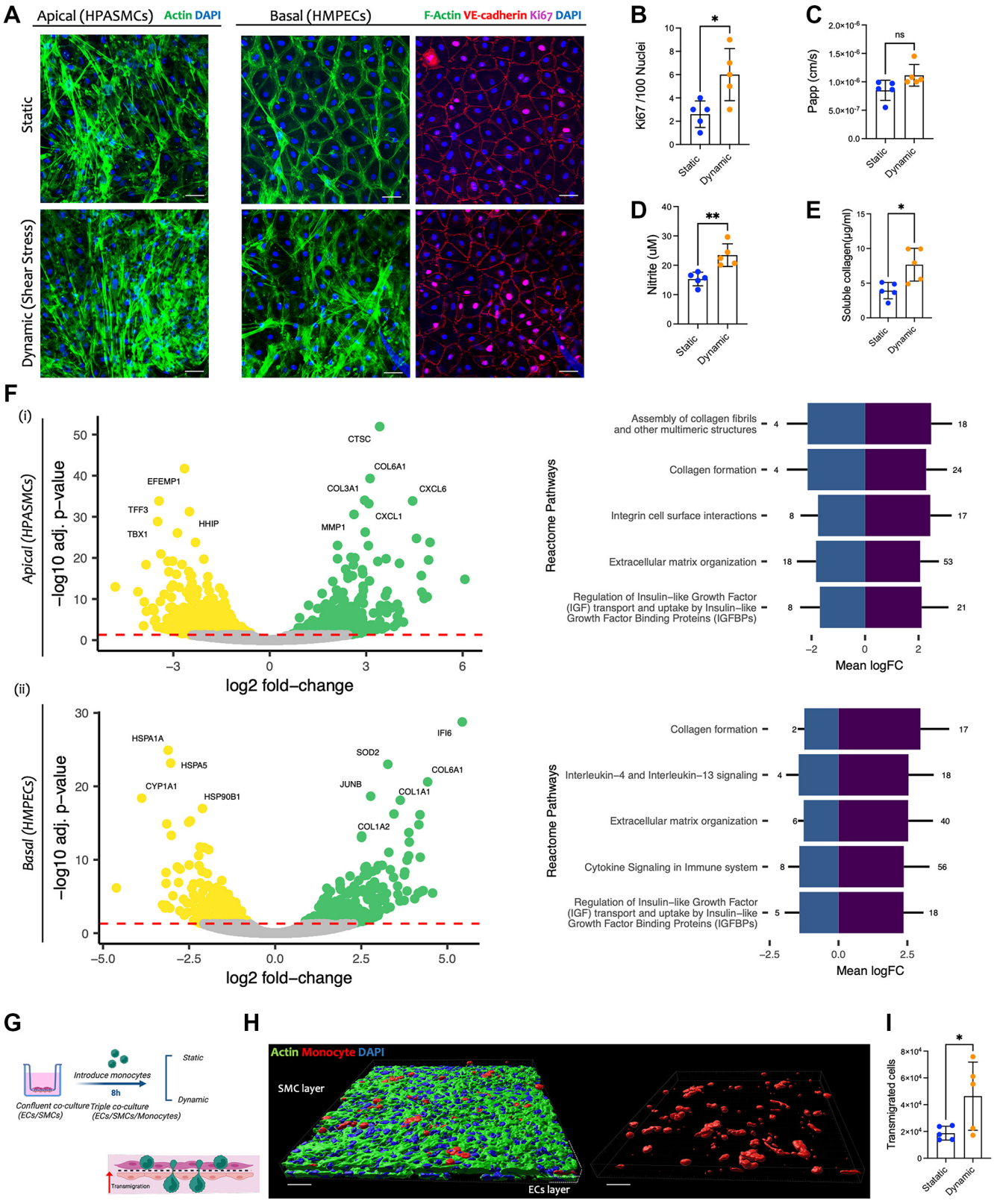

model disease-relevant transitions and enhance the translational relevance of the platform.

Based on previous characterizations of wall shear stress in pediatric patients with pulmonary arterial hypertension, wall shear stress in distal small pulmonary arteries (diameters 50–500 μm) ranged from 6.3 to 15.8 dyn/cm^2, depending on disease severity (16). Accordingly, we selected a wall shear stress of ~10.9 dyn/cm^2 at a perfusion rate of 2mL/min, a value consistent with previously published models for human pulmonary endothelial cells (17).

Leveraging the PIPE system, we identified early (8 h) shear stress-induced responses in endothelial cells consistent with initial features of PVD in PLD. We detected increases in the proliferation marker Ki67, nitrite release, and soluble collagen without evidence of overt cytotoxicity or barrier disruption compared with static (no-flow) conditions (Fig. 2, *A*–*E*). Complementing these findings, transcriptomic profiling of the coculture demonstrated strong regulation of pathways associated with ECM deposition and intercellular crosstalk (Fig. 2*F*). The regulation of *HSP90*, *CAVIN2,* and *CYP1A1* indicated a cellular stress response related to (*TGFB1*-dependent) transdifferentiation in hPMECs as previously described (32–35). In line with these findings, Reactome database analysis highlighted the regulation of inflammation and matrix formation in hPSMCs, indicated by the upregulation of *TGFB1*, *ILB1,* and *COL6A* transcription and accompanied by the downregulation of *TBX1*, known for its critical functions in vascular development (36). The identified mechanisms that characterize early injury hold potential for the development of therapeutic strategies (37, 38).

Expanding the system to a triple coculture of hPMECs, hPASMCs, and circulating THP-1 monocytes enabled modeling of early innate immunovascular interactions reflective of the inflammatory milieu characterizing neonatal lung disease (19). By the use of our biomimetic platform, we demonstrate that shear stress promoted monocyte recruitment and transmigration across the endothelial layer toward the hPASMC compartment, recapitulating early inflammatory infiltration (Fig. 2, *G*–*I*).

Despite extensive evidence that hyperoxia contributes to lung vascular pathology (9), the combined influence of clinically relevant oxygen ranges and shear stress has remained incompletely characterized. To address the impact of clinically prevalent treatments in a double hit model, we examined the combined effects of shear stress and graded hyperoxia (39, 40) (Fig. 3). Even brief exposure to severe hyperoxia ($F_{I_{O_2}}$ = 0.85) markedly impaired EC-SMC function in a dose-dependent manner (Fig. 3, *B*–*I*), consistent with clinical and preclinical observations in neonates and mice (28, 41). Severe hyperoxia increased ROS generation, enhanced THP-1 transmigration, activated caspase-3-dependent apoptosis, and elevated total soluble collagen production. Notably, collagen IV remained unchanged across conditions, indicating that basement membrane remodeling had not yet occurred within this acute (8 h) exposure window (Fig. 3*H*). Although moderate hyperoxia has been shown to induce ECM remodeling in human fetal airway SMCs (42), our observations reveal a more pronounced early response in the pulmonary vascular compartment with an increase in total soluble collagen without parallel changes in collagen IV, likely reflecting rapid initiation of ECM synthesis before deposition of more structured basement membrane-associated collagens.

In contrast to the dramatic changes induced by severe hyperoxia, moderate hyperoxia did not provoke changes in the outlined indicators of endothelial cell injury. Highlighting this important difference in the effect of oxygen concentrations on the vascular wall, future studies should address the clinically relevant aim to more adequately target the delicate balance between the beneficial (vasodilatory) (9, 43) and detrimental effects of oxygen supplementation with the potential to either mitigate or amplify shear stress-induced injury. However, the absence of active CO_2 control during oxygen exposure experiments and the use of atmospheric $F_{I_{O_2}}$ (0.21) as a reference condition may not fully recapitulate physiological conditions, as standard culture systems can provoke relative hyperoxia due to dissolved oxygen tensions as compared with the pulmonary microenvironment.

In summary, our study presents a platform that allows the description of critical early effects of clinically prevalent conditions on the vascular wall. Our study detailed the detrimental effects of increased shear stress, including the identification of candidate pathways that can inform future therapeutic approaches in BPD-associated PVD. The platform enabled the delineation of added injury mechanisms, such as hyperoxia under biologically relevant flow conditions, while incorporating the important role of the immune system, demonstrating their interaction with the vascular wall. Compared with conventional in vitro cultures that are based on static, mostly monocultural or selected coculture models, the PIPE platform enables the combination of controlled flow conditions with multicellular cocultures, including the circulation of immune cells. The model that

Figure 2. Comparative effects of dynamic shear stress vs. static culture on cellular responses. *A*: CLSM images of the coculture model showing F-actin cytoskeleton (phalloidin, *green*) and nuclei (DAPI, *blue*) on both the apical (hPASMC) and basal (hPMEC) surfaces. The basal endothelial layer additionally shows VE-cadherin (*red*) and Ki67 (*magenta*) staining. Scale bar: 50 μm. *B* and *C*: quantification of endothelial cell proliferation (Ki67$^+$ cells, *magenta*) (*B*) and apparent permeability (P_{app}) (*C*) under static vs. dynamic shear stress (10.9 dyn/cm^2, 8 h). *D* and *E*: analysis of nitrite secretion (*D*), measured by Griess assay and total soluble collagen content (*E*) in coculture models exposed to static or dynamic conditions. *F*: transcriptomic profiling of shear stress-exposed cocultures using 3′ massive analysis of cDNA ends (MACE) RNA sequencing. Volcano plots (*left*) display differentially expressed genes in (*i*) hPASMCs (apical side) and (*ii*) hPMECs (basal side), with upregulated genes shown in green and downregulated genes in yellow. Box plots (*right*) summarize mean expression levels of the top five significantly enriched biological pathways (upregulated and downregulated) in hPASMCs ($P < 0.05$, $n = 3$). *G*: schematic of the triple coculture setup in which THP-1 monocytic cells were added to the basal compartment of the hPMEC/hPASMC coculture and exposed to either static or shear stress conditions for 8 h. *H*: surface-rendered immunofluorescence images of the triple coculture model showing transmigration of THP-1 monocytes (*red*) from the basal endothelial layer toward the apical smooth muscle layer. Scale bar: 50 μm. *I*: quantification of transmigrated THP-1 monocytes. Data are presented as means ± SD ($n = 5$ biological replicates) and were analyzed using an unpaired *t* test. *$P < 0.05$, **$P < 0.01$. CLSM, confocal laser scanning microscopy; DAPI, 4′, 6-diamidino-2-phenylindole; hPASMC, human pulmonary arterial smooth muscle cell; hPMEC, human pulmonary microvascular endothelial cell. Figure created with a licensed version of BioRender.com.

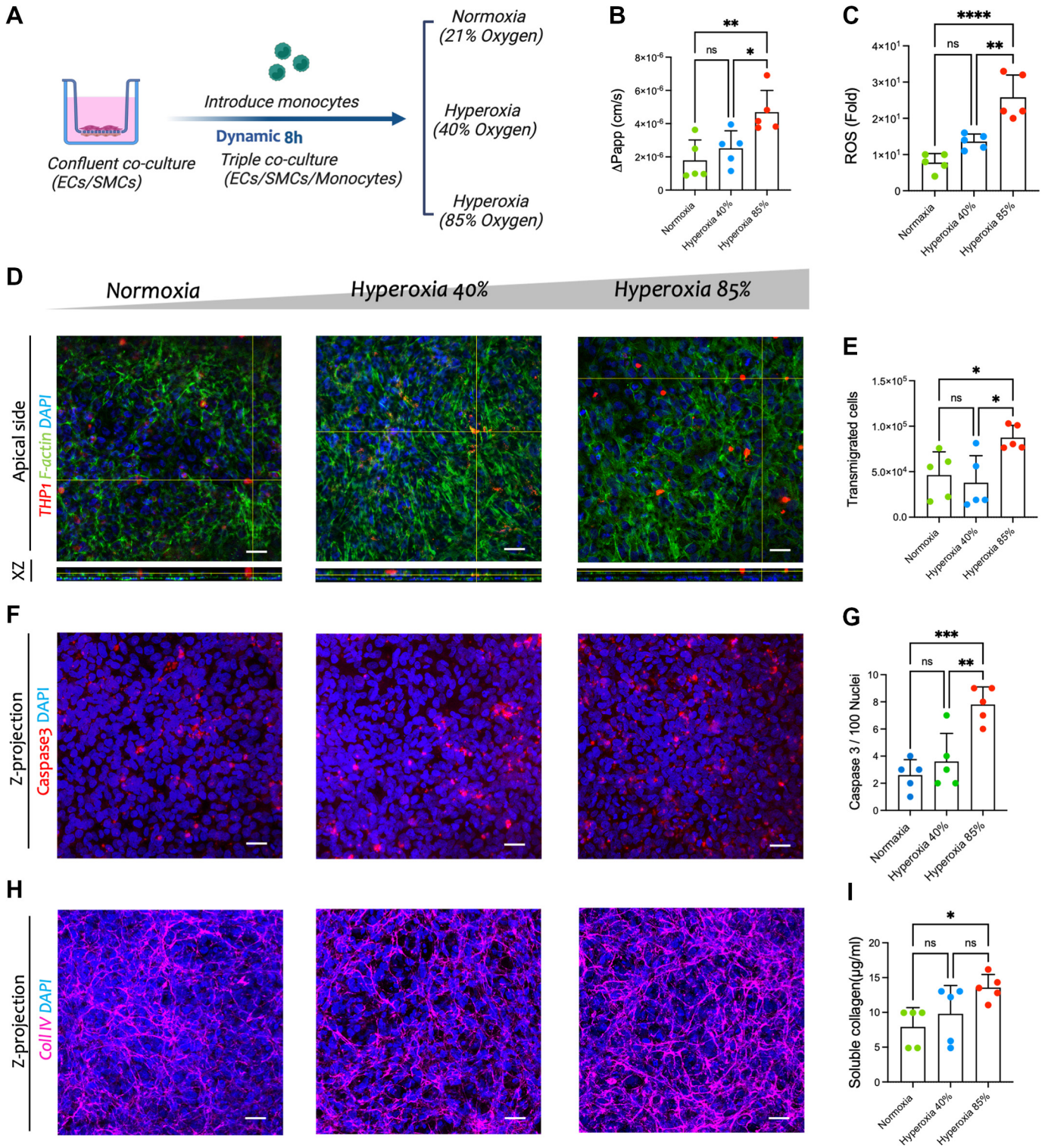

Figure 3. Effects of distinct oxygen concentrations on cell behavior under dynamic culture conditions. *A*: schematic of the triple coculture system (hPMECs/hPASMCs/THP-1) exposed to static or shear stress conditions and three oxygen environments: (21% O_2), moderate hyperoxia (40% O_2), and severe hyperoxia (85% O_2). *B–D*: evaluation of barrier function and oxidative stress responses; apparent permeability (*B*); intracellular reactive oxygen species (ROS) levels (*C*); orthogonal immunofluorescence confocal images of the triple coculture model showing F-actin (phalloidin, *green*), nuclei (DAPI, blue), and CMTPX-labeled THP-1 monocytes (*red*) (*D*). Scale bar: 50 μm. *E*: quantification of THP-1 monocytic cell movement and localization within the hPMEC/hPASMC coculture, tracked using CellTracker Red CMTPX. *F–H*: immunofluorescence Z-projection images showing qualitative (*F*) and quantitative (*G*) analysis of caspase-3 (red), and (*H*) collagen IV (magenta) expression within the triple coculture model. Scale bar: 50 μm. *I*: total soluble collagen content measured in culture supernatants. Data are presented as means ± SD ($n = 5$ biological replicates) and analyzed using two-way ANOVA with Tukey's multiple comparisons test. $^*P < 0.05$, $^{**}P < 0.01$, $^{***}P < 0.001$, $^{****}P < 0.0001$. DAPI, 4′,6-diamidino-2-phenylindole; hPASMC, human pulmonary arterial smooth muscle cell; hPMEC, human pulmonary microvascular endothelial cell. Figure created with a licensed version of BioRender.com.

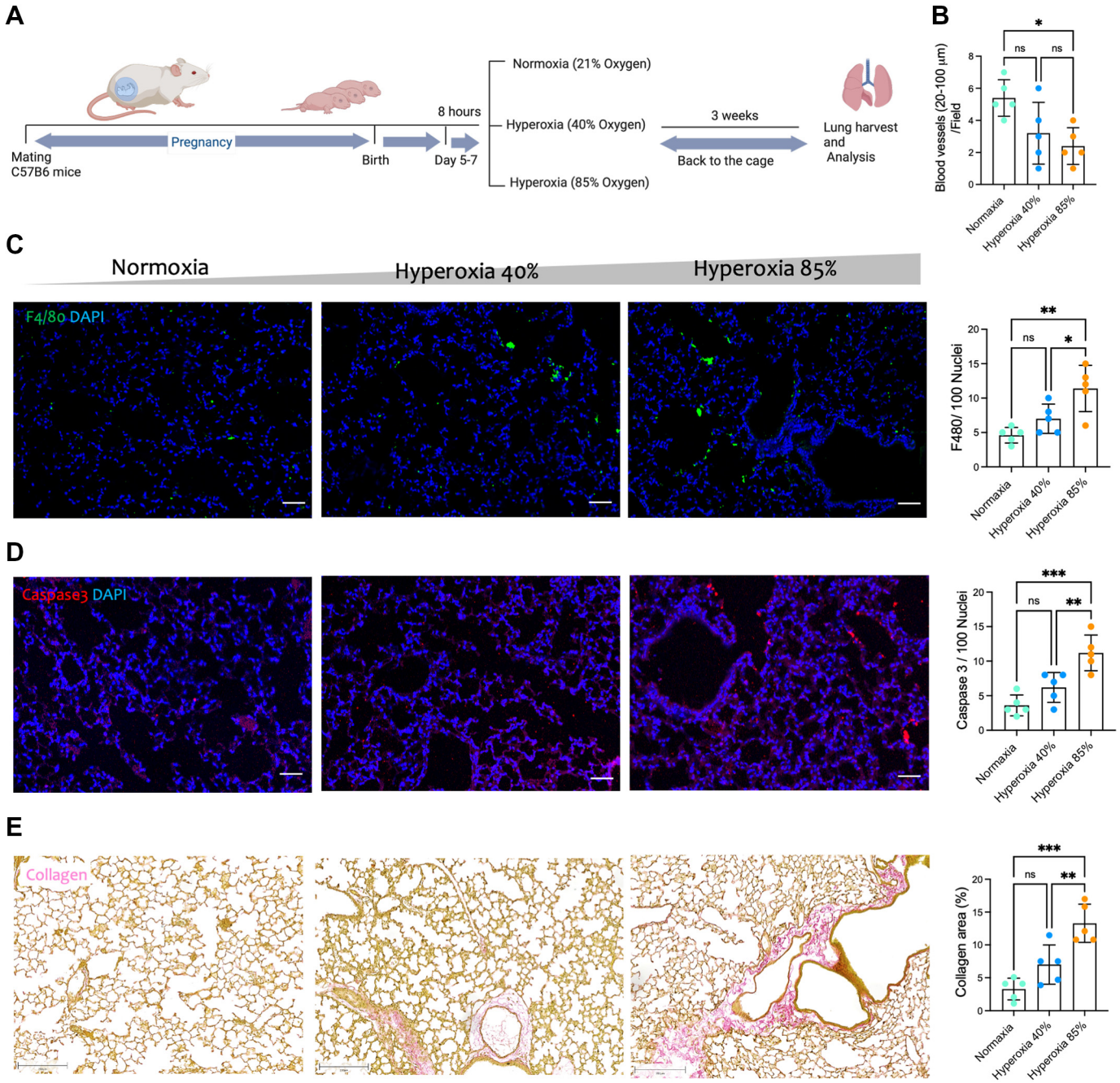

Figure 4. In vivo evaluation of moderate and severe hyperoxia-induced lung injury. *A*: schematic of the neonatal mouse model in which neonatal mice were exposed for 8 h to room air (normoxia), moderate hyperoxia ($FI_{O_2} = 0.40$; 40% O_2), or severe hyperoxia ($FI_{O_2} = 0.85$; 85% O_2) to induce acute lung injury. *B*: quantification of pulmonary microvessel density (20–100 µm diameter) in lung tissue sections. *C* and *D*: representative immunofluorescence images showing macrophage infiltration (F4/80, *C*) and apoptotic activity (caspase-3, *D*). Scale bar: 50 µm. *E*: qualitative and quantitative analysis of collagen deposition using Van Gieson staining, where collagen fibers appear pink, nuclei dark brown, and cytoplasm yellow. Scale bar: 500 µm. Data are presented as means ± SD ($n = 5$ individual mice) and were analyzed using one-way ANOVA with Tukey's multiple comparisons test. $^*P < 0.05$, $^{**}P < 0.01$, $^{***}P < 0.001$. FI_{O_2}, fraction of inspired oxygen. Figure created with a licensed version of BioRender.com.

can be scaled to multiple-hit conditions allows the interrogation of cell-cell interaction dynamics under the impact of defined mechanical and biochemical stressors (44–47). Although the PIPE platform does not recapitulate mechanical ventilation in the sense of alveolar stretch, it is important to note that shear stress in vivo is impacted by mechanical ventilation, especially in the preterm infant where the significant levels of positive end-expiratory pressure (PEEP) as well as inhomogeneous ventilation with a side-by-side of overinflation and atelectasis recurrently add to changes in pressure and blood in the developing lung, provoking strain. The alteration of intrathoracic pressure and ventilation-dependent changes in pulmonary vascular resistance and blood flow distribution contribute to endothelial activation

and vascular remodeling (48). As such, PIPE provides a biomimetic platform that may enhance in vitro to in vivo translation (49). Supporting the translational relevance, we confirmed the immune-driven characteristics of lung injury in a preclinical BPD mouse model and the persistence of these changes beyond alveolarization (10, 25).

Taken together, our PIPE model—integrating mechanical forces into a double-hit model when adding oxidative stress while allowing to study immune cell interactions—offers a controlled and reductionist in vitro system that captures key aspects of the pulmonary microvascular responses to injury and surpasses static or single-parameter culture models in translational relevance. Although the PIPE platform mirrors hallmarks of early endothelial injury provoked by shear stress and hyperoxia in the neonatal mouse lung, it does not fully capture the in vivo complexity of the gas-exchange region, including the multilayered alveolar architecture and epithelial-endothelial interactions. Incorporating additional cellular layers will be important to better recapitulate the alveolar interface and to study interaction mechanisms relevant to the developing lung. Further integration of in vivo-like features or advanced imaging approaches will be required to validate and extend these findings. Future work will also benefit from extending exposure duration, optimizing coculture media (50), validating cell-type-specific transcriptomes under migratory conditions, and incorporating additional neonatal-relevant therapeutic interventions such as retinoic acid or nitric oxide (51, 52).

DATA AVAILABILITY

All data generated and analyzed during the current study are available from the corresponding author on request.

ACKNOWLEDGMENTS

The authors thank Andreas Schroeppel, Elisabeth Schindler, and Susanne Mehring for technical assistance. Figures created with a licensed version of BioRender.com.

GRANTS

This work was supported by the Young Investigator Grant NWG VH-NG-829 from the Helmholtz Foundation and the Helmholtz Zentrum München, Germany; the International Research Group "Role of BMP signaling" (01KI07110), Helmholtz Foundation [Federal Ministry of Education and Research in Germany (BMBF)]; the German Center for Lung Research (DZL), and the Research Training Group "Targets in Toxicology" (GRK2338) of the German Science and Research Organization (DFG). This work was also supported by the Deutsche Forschungsgemeinschaft (DFG, German Research Foundation)—TRR 359—Project No. 491676693 and by the Chan Zuckerberg Initiative (Mapping the Pediatric Inhalation Interface: Nose, Mouth, and Airways). Additional financial support was provided by the Stiftung AtemWeg (LSS AIRR). As a member of the PVRI GoDeep Registry (PVRI Global Deep Phenotyping PH Meta-Registry), the study was supported through intellectual contribution. Ali Doryab was supported by the Walter Benjamin Postdoctoral Fellowship from the Deutsche Forschungsgemeinschaft (DFG, German Research Foundation; Project No. 524039583).

DISCLOSURES

No conflicts of interest, financial or otherwise, are declared by the authors.

AUTHOR CONTRIBUTIONS

M.H., A.D., O.S., and A.H. conceived and designed research; M.H., A.D., and A.H. performed experiments; M.H., A.D., J.H., B.S., and A.H. analyzed data; M.H., A.D., J.H., B.S., and A.H. interpreted results of experiments; M.H. and A.H. prepared figures; M.H., A.D., and A.H. drafted manuscript; M.H., A.D., B.S., and A.H. edited and revised manuscript; M.H., B.S., and A.H. approved final version of manuscript.

REFERENCES

1. **Ohuma EO**, **Moller AB**, **Bradley E**, **Chakwera S**, **Hussain-Alkhateeb L**, **Lewin A**, **Okwaraji YB**, **Mahanani WR**, **Johansson EW**, **Lavin T**, **Fernandez DE**, **Domínguez GG**, **de Costa A**, **Cresswell JA**, **Krasevec J**, **Lawn JE**, **Blencowe H**, **Requejo J**, **Moran AC.** National, regional, and global estimates of preterm birth in 2020, with trends from 2010: a systematic analysis. *Lancet* 402: 1261–1271, 2023 [Erratum in *Lancet* 403: 618, 2024]. doi:10.1016/S0140-6736(23)00878-4.
2. **Jobe AJ.** The new BPD: an arrest of lung development. *Pediatr Res* 46: 641–643, 1999. doi:10.1203/00006450-199912000-00007.
3. **Sahni M**, **Bhandari V.** Patho-mechanisms of the origins of bronchopulmonary dysplasia. *Mol Cell Pediatr* 8: 21, 2021. doi:10.1186/s40348-021-00129-5.
4. **Guo X**, **Ma D**, **Li R**, **Zhang R**, **Guo Y**, **Yu Z**, **Chen C.** Association between viral infection and bronchopulmonary dysplasia in preterm infants: a systematic review and meta-analysis. *Eur J Pediatr* 183: 2965–2981, 2024. doi:10.1007/s00431-024-05565-9.
5. **Course CW**, **Bush A**, **Kotecha S.** Looking beyond bronchopulmonary dysplasia: prematurity-associated lung disease and its phenotypes. *Lancet Respir Med* 14: 60–71, 2026. doi:10.1016/S2213-2600(25)00372-8.
6. **Hilgendorff A**, **Reiss I**, **Ehrhardt H**, **Eickelberg O**, **Alvira CM.** Chronic lung disease in the preterm infant. lessons learned from animal models. *Am J Respir Cell Mol Biol* 50: 233–245, 2014. doi:10.1165/rcmb.2013-0014TR.
7. **Hansmann G**, **Sallmon H**, **Roehr CC**, **Kourembanas S**, **Austin ED**, **Koestenberger M**; **European Pediatric Pulmonary Vascular Disease Network (EPPVDN).** Pulmonary hypertension in bronchopulmonary dysplasia. *Pediatr Res* 89: 446–455, 2021. doi:10.1038/s41390-020-0993-4.
8. **Häfner F**, **Kindt A**, **Strobl K**, **Förster K**, **Heydarian M**, **Gonzalez E**, **Schubert B**, **Kraus Y**, **Dalla Pozza R**, **Flemmer AW**, **Ertl-Wagner B**, **Dietrich O**, **Stoecklein S**, **Tello K**, **Hilgendorff A.** MRI pulmonary artery flow detects lung vascular pathology in preterms with lung disease. *Eur Respir J* 62: 2202445, 2023. doi:10.1183/13993003.02445-2022.
9. **Giusto K**, **Wanczyk H**, **Jensen T**, **Finck C.** Hyperoxia-induced bronchopulmonary dysplasia: better models for better therapies. *Dis Model Mech* 14: dmm047753, 2021. doi:10.1242/dmm.047753.
10. **Heydarian M**, **Oak P**, **Zhang X**, **Kamgari N**, **Kindt A**, **Koschlig M**, **Pritzke T**, **Gonzalez-Rodriguez E**, **Förster K**, **Morty RE**, **Häfner F**, **Hübener C**, **Flemmer AW**, **Yildirim AO**, **Sudheendra D**, **Tian X**, **Petrera A**, **Kirsten H**, **Ahnert P**, **Morrell N**, **Desai TJ**, **Sucre J**, **Spiekerkoetter E**, **Hilgendorff A.** Relationship between impaired BMP signalling and clinical risk factors at early-stage vascular injury in the preterm infant.*Thorax* 77: 1176–1186, 2022. doi:10.1136/thoraxjnl-2021-218083.
11. **Cool CD**, **Kuebler WM**, **Bogaard HJ**, **Spiekerkoetter E**, **Nicolls MR**, **Voelkel NF.** The hallmarks of severe pulmonary arterial hypertension: the cancer hypothesis—ten years later. *Am J Physiol Lung Cell Mol Physiol* 318: L1115–L1130, 2020. doi:10.1152/ajplung.00476.2019.
12. **Mourani PM**, **Abman SH.** Pulmonary vascular disease in bronchopulmonary dysplasia. *Curr Opin Pediatr* 25: 329–337, 2013. doi:10.1097/MOP.0b013e328360a3f6.

13. **Wang H**, **Jafri A**, **Martin RJ**, **Nnanabu J**, **Farver C**, **Prakash YS**, **MacFarlane PM.** Severity of neonatal hyperoxia determines structural and functional changes in developing mouse airway. *Am J Physiol Lung Cell Mol Physiol* 307: L295–L301, 2014. doi:10.1152/ajplung.00208.2013.
14. **Attaye I**, **Smulders YM**, **de Waard MC**, **Oudemans-van Straaten HM**, **Smit B**, **Van Wijhe MH**, **Musters RJ**, **Koolwijk P**, **Spoelstra-de Man AME.** The effects of hyperoxia on microvascular endothelial cell proliferation and production of vaso-active substances. *Intensive Care Med Exp* 5: 22, 2017. doi:10.1186/s40635-017-0135-4.
15. **D'Amore PA**, **Sweet E.** Effects of hyperoxia on microvascular cells in vitro. *In Vitro Cell Dev Biol* 23: 123–128, 1987. doi:10.1007/BF02623592.
16. **Yang W**, **Dong M**, **Rabinovitch M**, **Chan FP**, **Marsden AL**, **Feinstein JA.** Evolution of hemodynamic forces in the pulmonary tree with progressively worsening pulmonary arterial hypertension in pediatric patients. *Biomech Model Mechanobiol* 18: 779–796, 2019. doi:10.1007/s10237-018-01114-0.
17. **Kostyunina DS**, **Rowan SC**, **Pakhomov NV**, **Dillon E**, **Rochfort KD**, **Cummins PM**, **O'Rourke MJ**, **McLoughlin P.** Shear stress markedly alters the proteomic response to hypoxia in human pulmonary endothelial cells. *Am J Respir Cell Mol Biol* 68: 551–565, 2023. doi:10.1165/rcmb.2022-0340OC.
18. **Windhorst AC**, **Heydarian M**, **Schwarz M**, **Oak P**, **Förster K**, **Frankenberger M**, **Gonzalez Rodriguez E**, **Zhang X**, **Ehrhardt H**, **Hübener C**, **Flemmer AW**, **Hossain H**, **Stoeger T**, **Schulz C**, **Hilgendorff A.** Monocyte signature as a predictor of chronic lung disease in the preterm infant. *Front Immunol* 14: 1112608–1112609, 2023 [Erratum in *Front Immunol* 14: 1209992, 2023]. doi:10.3389/fimmu.2023.1112608.
19. **Heydarian M**, **Schulz C**, **Stoeger T**, **Hilgendorff A.** Association of immune cell recruitment and BPD development. *Mol Cell Pediatr* 9: 16, 2022. doi:10.1186/s40348-022-00148-w.
20. **Schermuly RT**, **Ghofrani HA**, **Wilkins MR**, **Grimminger F.** Mechanisms of disease: pulmonary arterial hypertension. *Nat Rev Cardiol* 8: 443–455, 2011. doi:10.1038/nrcardio.2011.87.
21. **Poon C.** Measuring the density and viscosity of culture media for optimized computational fluid dynamics analysis of in vitro devices. *J Mech Behav Biomed Mater* 126: 105024, 2022. doi:10.1016/j.jmbbm.2021.105024.
22. **Doryab A**, **Taskin MB**, **Stahlhut P**, **Groll J**, **Schmid O.** Real-time measurement of cell mechanics as a clinically relevant readout of an in vitro lung fibrosis model established on a bioinspired basement membrane. *Adv Mater* 34: e2205083, 2022. doi:10.1002/adma.202205083.
23. **Hubatsch I**, **Ragnarsson EGE**, **Artursson P.** Determination of drug permeability and prediction of drug absorption in Caco-2 monolayers. *Nat Protoc* 2: 2111–2119, 2007. doi:10.1038/nprot.2007.303.
24. **Schindelin J**, **Arganda-Carreras I**, **Frise E**, **Kaynig V**, **Longair M**, **Pietzsch T**, **Preibisch S**, **Rueden C**, **Saalfeld S**, **Schmid B**, **Tinevez JY**, **White DJ**, **Hartenstein V**, **Eliceiri K**, **Tomancak P**, **Cardona A.** Fiji: an open-source platform for biological-image analysis. *Nat Methods* 9: 676–682, 2012. doi:10.1038/nmeth.2019.
25. **Hussain M**, **Xu C**, **Ahmad M**, **Yang Y**, **Lu M**, **Wu X**, **Tang L**, **Wu X.** Notch signaling: linking embryonic lung development and asthmatic airway remodeling. *Mol Pharmacol* 92: 676–693, 2017. doi:10.1124/mol.117.110254.
26. **Oak P**, **Pritzke T**, **Thiel I**, **Koschlig M**, **Mous DS**, **Windhorst A**, **Jain N**, **Eickelberg O**, **Foerster K**, **Schulze A**, **Goepel W**, **Reicherzer T**, **Ehrhardt H**, **Rottier RJ**, **Ahnert P**, **Gortner L**, **Desai TJ**, **Hilgendorff A.** Attenuated PDGF signaling drives alveolar and microvascular defects in neonatal chronic lung disease. *EMBO Mol Med* 9: 1504–1520, 2017. doi:10.15252/emmm.201607308.
27. **Balink S**, **Onland W**, **Vrijlandt EJLE**, **Andrinopoulou E-R**, **Bos AF**, **Dijk PH**, **Goossens L**, **Hulsmann AR**, **Nuytemans DH**, **Reiss IKM**, **Sprij AJ**, **Kroon AA**, **van Kaam AH**, **Pijnenburg M**, **SOS BPD study group.** Supplemental oxygen strategies in infants with bronchopulmonary dysplasia after the neonatal intensive care unit period: study protocol for a randomised controlled trial (SOS BPD study). *BMJ Open* 12: e060986, 2022. doi:10.1136/bmjopen-2022-060986.
28. **Enomoto M**, **Gosal K**, **Cubells E**, **Escobar J**, **Vento M**, **Jankov RP**, **Belik J.** Sex-dependent changes in the pulmonary vasoconstriction potential of newborn rats following short-term oxygen exposure. *Pediatr Res* 72: 468–478, 2012. doi:10.1038/pr.2012.120.
29. **Mourani PM**, **Abman SH.** Pulmonary hypertension and vascular abnormalities in bronchopulmonary dysplasia. *Clin Perinatol* 42: 839–855, 2015. doi:10.1016/j.clp.2015.08.010.
30. **Puchwein-Schwepcke A**, **Grzybowski AK**, **Genzel-Boroviczény O**, **Nussbaum C.** Effects of prematurity on the cutaneous microcirculatory network in the first weeks of life. *Front Pediatr* 7: 198–199, 2019. doi:10.3389/fped.2019.00198.
31. **Doryab A**, **Schmid O.** Towards a gold standard functional readout to characterize in vitro lung barriers. *Eur J Pharm Sci* 179: 106305, 2022. doi:10.1016/j.ejps.2022.106305.
32. **Malikova E**, **Kmecova Z**, **Doka G**, **Pivackova LB**, **Balis P**, **Trubacova S**, **Velasova E**, **Krenek P**, **Klimas J.** Pioglitazone restores phosphorylation of downregulated caveolin-1 in right ventricle of monocrotaline-induced pulmonary hypertension. *Clin Exp Hypertens* 44: 101–112, 2022. doi:10.1080/10641963.2021.1996589.
33. **Nakano N**, **Sakata N**, **Katsu Y**, **Nochise D**, **Sato E**, **Takahashi Y**, **Yamaguchi S**, **Haga Y**, **Ikeno S**, **Motizuki M**, **Sano K**, **Yamasaki K**, **Miyazawa K**, **Itoh S.** Dissociation of the AhR/ARNT complex by TGF-β/Smad signaling represses *CYP1A1* gene expression and inhibits benze[a]pyrene-mediated cytotoxicity. *J Biol Chem* 295: 9033–9051, 2020. doi:10.1074/jbc.RA120.013596.
34. **Patil MN**, **Datkhile KD**, **Gudur AK**, **Gudur RA**, **Patil SR.** Single-nucleotide polymorphism in CYP1A1, CYP1B1, CYP2B6, CYP2C8, and CYP2C9 genes and their association with gastrointestinal cancer: a hospital-based case-control study. *J Cancer Res Ther* 20: 216–223, 2024. doi:10.4103/jcrt.jcrt_294_22.
35. **Higuchi Y**, **Ogata T**, **Nakanishi N**, **Nishi M**, **Tsuji Y**, **Tomita S**, **Conway SJ**, **Matoba S.** Cavin-2 promotes fibroblast-to-myofibroblast trans-differentiation and aggravates cardiac fibrosis. *ESC Heart Fail* 11: 167–178, 2024. doi:10.1002/ehf2.14571.
36. **Ramirez A**, **Vyzas CA**, **Zhao H**, **Eng K**, **Degenhardt K**, **Astrof S.** Buffering mechanism in aortic arch artery formation and congenital heart disease. *Circ Res* 134: e112–e132, 2024. doi:10.1161/CIRCRESAHA.123.322767.
37. **Lin X**, **Liu W**, **Chu Y**, **Zhang H**, **Zeng L**, **Lin Y**, **Kang K**, **Peng F**, **Lin J**, **Huang C**, **Chai D.** Activation of AHR by ITE improves cardiac remodelling and function in rats after myocardial infarction. *ESC Heart Fail* 10: 3622–3636, 2023. doi:10.1002/ehf2.14532.
38. **Moon J**, **Zhou H**, **Zhang L**, **Tan W**, **Liu Y**, **Zhang S**, **Morlock LK**, **Bao X**, **Palecek SP**, **Feng JQ**, **Williams NS**, **Amatruda JF**, **Olson EN**, **Bassel-Duby R**, **Lum L.** Blockade to pathological remodeling of infarcted heart tissue using a porcupine antagonist. *Proc Natl Acad Sci USA* 114: 1649–1654, 2017. doi:10.1073/pnas.1621346114.
39. **Kapadia V**, **Oei JL.** Optimizing oxygen therapy for preterm infants at birth: are we there yet? *Semin Fetal Neonatal Med* 25: 101081, 2020. doi:10.1016/j.siny.2020.101081.
40. **Welsford M**, **Nishiyama C**, **Shortt C**, **Weiner G**, **Roehr CC**, **Isayama T**, **Dawson JA**, **Wyckoff MH**, **Rabi Y**; **International Liaison Committee on Resuscitation Neonatal Life Support Task Force.** Initial oxygen use for preterm newborn resuscitation: a systematic review with meta-analysis. *Pediatrics* 143: e20181828, 2019. doi:10.1542/peds.2018-1828.
41. **Kumar VHS**, **Wang H**, **Nielsen L.** Short-term perinatal oxygen exposure may impair lung development in adult mice. *Biol Res* 53: 51, 2020. doi:10.1186/s40659-020-00318-y.
42. **Vogel ER**, **Britt RD**, **Faksh A**, **Kuipers I**, **Pandya H**, **Prakash YS**, **Martin RJ**, **Pabelick CM.** Moderate hyperoxia induces extracellular matrix remodeling by human fetal airway smooth muscle cells. *Pediatr Res* 81: 376–383, 2017. doi:10.1038/pr.2016.218.
43. **Twisselmann N**, **Pagel J**, **Künstner A**, **Weckmann M**, **Hartz A**, **Glaser K**, **Hilgendorff A**, **Göpel W**, **Busch H**, **Herting E**, **Weinberg JB**, **Härtel C.** Hyperoxia/hypoxia exposure primes a sustained pro-inflammatory profile of preterm infant macrophages upon LPS stimulation. *Front Immunol* 12: 762789–762720, 2021. doi:10.3389/fimmu.2021.762789.
44. **Sebastián-Jaraba IS**, **Fernández-Gómez MJ**, **Blázquez-Serra R**, **Sanz-Andrea S**, **Blanco-Colio LM**, **Méndez-Barbero N.** In vitro 3D co-culture model of human endothelial and smooth muscle cells to study pathological vascular remodeling. *Clín Invest Arterioscler* 36: 356–363, 2024. doi:10.1016/j.artere.2024.11.004.
45. **Boehme J**, **Sun X**, **Tormos KV**, **Gong W**, **Kellner M**, **Datar SA**, **Kameny RJ**, **Yuan JXJ**, **Raff GW**, **Fineman JR**, **Black SM**, **Maltepe E.** Pulmonary artery smooth muscle cell hyperproliferation and metabolic shift triggered by pulmonary overcirculation. *Am J Physiol*

Heart Circ Physiol 311: H944–H957, 2016. doi:10.1152/ajpheart.00040.2016.

46. **Morii C**, **Tanaka HY**, **Izushi Y**, **Nakao N**, **Yamamoto M**, **Matsubara H**, **Kano MR**, **Ogawa A.** 3D in vitro model of vascular medial thickening in pulmonary arterial hypertension. *Front Bioeng Biotechnol* 8: 482, 2020. doi:10.3389/fbioe.2020.00482.
47. **Lavender MD**, **Pang Z**, **Wallace CS**, **Niklason LE**, **Truskey GA.** A system for the direct co-culture of endothelium on smooth muscle cells. *Biomaterials* 26: 4642–4653, 2005. doi:10.1016/j.biomaterials.2004.11.045.
48. **Conhaim RL**, **Segal GS**, **Watson KE.** Positive pressure ventilation compresses pulmonary acinar microvessels but not their supply vessels. *Microvasc Res* 122: 71–77, 2019. doi:10.1016/j.mvr.2018.11.008.
49. **Doryab A**, **Groll J.** Biomimetic in vitro lung models: current challenges and future perspective. *Adv Mater* 35: e2210519, 2023. doi:10.1002/adma.202210519.
50. **Vis MAM**, **Ito K**, **Hofmann S.** Impact of culture medium on cellular interactions in in vitro co-culture systems. *Front Bioeng Biotechnol* 8: 911, 2020. doi:10.3389/fbioe.2020.00911.
51. **Meyer S**, **Bay J**, **Franz AR**, **Erhardt H**, **Klein L**, **Petzinger J**; **NeoVitaA trial investigators, et al.** Early postnatal high-dose fat-soluble enteral vitamin A supplementation for moderate or severe bronchopulmonary dysplasia or death in extremely low birthweight infants (NeoVitaA): a multicentre, randomised, parallel-group, double-blind, placebo-controlled, investigator-initiated phase 3 trial. *Lancet Respir Med* 12: 544–555, 2024 [Erratum in *Lancet Respir Med* 12: e42, 2024]. doi:10.1016/S2213-2600(24)00073-0.
52. **Häfner F**, **Johansson C**, **Schwarzkopf L**, **Förster K**, **Kraus Y**, **Flemmer AW**, **Hansmann G**, **Sallmon H**, **Felderhoff-Müser U**, **Witt S**, **Schwettmann L**, **Hilgendorff A.** Current diagnosis and treatment practice for pulmonary hypertension in bronchopulmonary dysplasia—a survey study in Germany (PUsH BPD). *Pulm Circ* 13: e12320, 2023. doi:10.1002/pul2.12320.